Molecular dynamics studies of silica wafer bonding

Dirk Timpel, Max Schaible, and Kurt Scheerschmidt[a)]
Max Planck Institute of Microstructure Physics, Weinberg 2, D-06120 Halle, Germany

(Received 31 August 1998; accepted for publication 1 December 1998)

Molecular dynamics simulations are performed to investigate the atomic processes initiated by the adhesion of two silica surfaces, which are covered with adsorbates of oxygen, hydrogen or water molecules. The calculations describe the mechanism of hydrophilic silicon wafer bonding in terms of empirical potentials assumed. The challenge of the macroscopically relevant computations is to understand and to predict the formation of covalent bonds as a function of initial silica structures, external forces, adsorbates, and annealing temperatures applied. © *1999 American Institute of Physics.* [S0021-8979(99)04005-0]

I. INTRODUCTION

According to the importance of wafer bonding for semiconductor electronics and micromechanic applications there is an increasing interest in better understanding the physical processes by theoretical analyses of the interaction of the atoms at the two surfaces in contact.[1,2] Wafer bonding was initially applied to bond fused quartz. Nowadays, the main interests in wafer bonding include the enhancement of the technique for silicon covered by silicon dioxide at low temperatures (100–400 °C), the prediction of the behavior of new materials, and to control all factors influencing the bonding process. While molecular dynamics (MD) simulations have successfully been used to describe ultrahigh-vacuum bonding experiments for Si(100) (Ref. 3) and hydrogen passivated hydrophobic bonding processes,[4] and to analyze the defect structure at bonded interfaces,[5] little has been reported on the bonding of amorphous silica (a-SiO_2) surfaces,[6] which may be the basis or a first step to describe hydrophilic wafer bonding. Referring to the empirical potentials established to investigate the influence of moisture on silica surfaces[7,8] and the behavior of particles in sodium silicate glasses,[9] the present paper theoretically deals with effects of structure modeling, annealing, surface coverage and external forces applied (restrictions) to transform the hydrogen bonding to covalent forces for silica to silica interfaces. As there are no empirical potentials to describe Si/SiO_2 interactions sufficiently well, our considerations are restricted to the direct interaction of two a-SiO_2 structures as models of thick native oxides or those thermally processed in special atmospheres replacing hydrophilic Si wafers.

The bulk and surface structure of silica have been studied quite extensively over the past years by different experimental techniques as well as theoretically by MD simulations. Mostly, silicon is tetrahedrally bonded to four oxygen neighbors in the crystalline silica c-SiO_2 polymorphs. a-SiO_2 glass is generally considered to be made up of SiO_4 tetrahedra linked by sharing oxygens. As the electronic properties are determined by the SiO_4 tetrahedra, parameter-free *ab initio* structure calculations were performed to understand the surface structure as, e.g., reordering processes, point defects, H termination and oxidation (see, for example, Refs. 10–13). *Ab initio* calculations of a few hundred atoms are now possible, which can be extended to larger structures by using tight-binding approximations. However, simulating macroscopically relevant structures as, e.g., for the bonding process, always requires a large number of particles (more than 10^4 atoms in extended supercells) to be considered and many-body empirical potentials to be applied, i.e., classical MD with suitable boundary conditions.

II. COMPUTATIONAL PROCEDURE

Classical molecular dynamics solves the equations of motion of an ensemble of particles assuming empirical interatomic potentials. The quality of all empirical methods, however, depends on a suitable parametrization of the potential, which should reflect both the SiO_4 tetrahedron structure of *ab initio* investigations and the bulk properties determined experimentally. The potential used here is the modified Born–Mayer–Huggins (BMH) ionic pair interaction combined with a weak three-body term.[7–9] The BMH interaction combines a repulsion and a Coulombic term, which is screened to avoid the long-range Ewald sums. The three-body term is similar to that initially developed by Stillinger and Weber (SW) for silicon.[14] In addition, a Rahman–Stillinger–Lemberg (RSL) term was used for the water interactions.[15] The parameters were fitted to describe liquid water and several configurations of silica with H_2O by comparing them with quantum-chemical calculations.[8,15,16] The O–O interactions are treated in the same way for both silica and water. There are other well-known potentials, e.g., the Tsuneyuki potential[17] fitting well the vibrational spectra or the Vashista potential[18] optimized for quartz and showing a better transferability.[19] The potentials were not only applied to structure calculations and to study the behavior of different modifications of quartz, cristobalite and tridymite with respect to the pressure-dependent phase transitions. They were also applied to the H diffusion and to study the liquid and fused phases. The BMH–SW–RSL potential of Garo-

a)Electronic mail: schee@mpi-halle.de

falini, however, is preferred here because of the better stability of tridymite and cristobalite, which may be the experimentally obtained structures at the Si/SiO_2 interfaces (see, e.g., Ref. 20 and compare with the present results of the stability of silica).

The calculations are performed using a constant volume (NVE ensemble) or a constant pressure (NpT ensemble). NVE is preferred for free surfaces and for simulations to calculate the diffusion constants, whereas NpT enables a relaxation of the cell dimensions and the application of an outer pressure, which is important for, e.g., the glass generation and the simulation of wafer interfaces, respectively. In order to control the system temperature either all particle velocities are slightly rescaled each time step or solely the outer layers of the structure model, still applying periodic boundary conditions parallel to the interfaces. In the latter case, the energy dissipation and thus the dynamic bonding behavior is controlled by the transfer rates of the kinetic energy at the borders of the model describing an energy flux into a macroscopic substrate. This improvement of the MD is important to wafer bonding because each new bond at the interface implies an energy gain on the order of eV, which is distributed to a small number of atoms probably resulting in a nonphysical melt of the surfaces in a constant-energy simulation.

III. RESULTS

A. Crystalline and amorphous silica

The generation of amorphous silica models starts from crystalline silica structures, as e.g., cristobalite, tridymite, or quartz, whereas coesite, stishovite, and keatite have not been tested in our simulations. The polymorphs are differentiated in the way in which the tetrahedra are linked or arranged (i.e., the Si–O–Si angle), and by the rings they form. They all display surprisingly similar cohesive energies;[21] however, the structures have been discussed quite controversially. Experimentally, β-cristobalite is stable above 1743 K at ambient pressures. The present calculations were made for NpT and NVE ensembles: The simulated crystal structures are stable at 0 K, i.e., the atomic movement can be characterized by a mean square displacement (MSD) of less than MSD $<3\times10^{-5}\,\mathrm{nm}^2$ and a corresponding dispersion (DSP) of the atomic displacement of less than DSP $<10^{-6}\,\mathrm{nm}^2$ with respect to the initial configuration. Constant pressure annealing below the glass transition temperature, however, transforms the initial structures into β-cristobalite (Fd3m, $a=0.713$ nm, supercell of 648 atoms, Si–O=0.155 nm, O–Si–O $=109.47°$, Si–O–Si$=179.99°$). The β-cristobalite is very stable showing MSD$\approx3.55\times10^{-9}\,\mathrm{nm}^2$ with DSP$=6.6\times10^{-10}\,\mathrm{nm}^2$. During the transformation process different metastable configurations can be created for different temperatures during the annealing process, strongly depending on the heating/cooling rates and the ensembles chosen. For instance, α-cristobalite is stable up to 40 K in both NVE and NpT simulations showing one or two structural transitions, respectively, before the final β-cristobalite is reached. The MSD and the DSP of the atomic displacements are also approximately proportional to the temperature when structural changes occur. Below 40 K α-cristobalite is characterized by MSD$\approx7\times10^{-5}\,\mathrm{nm}^2$ with DSP$=8\times10^{-6}\,\mathrm{nm}^2$, which indicates a small change of the Si–O–Si angle in contrast to the perfect stability of β-cristobalite. However, whereas NpT simulations yield a rapid 14% volume enlargement at about 45 K and result in the final β-cristobalite passing one metastable structure, the structural transition for the constant volume simulation remains incomplete and leads to a noncrystallographic configuration with MSD$\approx0.009\,\mathrm{nm}^2$ but DSP $=0.0011\,\mathrm{nm}^2$. Structural changes are always reversible only if the structure fits the cubic supercell in the MD simulation sufficiently well, which is not valid, e.g., for all quartz modifications. For the sake of simplicity, the β-tridymite high-temperature Wyckoff model[22,23] ($P6_3/\mathrm{mmc}$, $a=0.503$ nm, $c=0.822$ nm, supercell of 648 atoms, Si–O$=0.154\pm0.002$ nm, O–Si–O$=109.14\pm0.81°$, Si–O–Si$=179.92\pm0.13°$; the variance is due to the insufficient fit of the supercell model after annealing below the glass transition temperature) was used as the basis of creating some of the amorphous silica glasses, too.

The molecular dynamics simulations of melting different crystalline silica structures applying a heating rate of 2×10^{14} K/s and cooling rates of 2×10^{13} K/s (see model N3P2 of Table I) show an annealing behavior similar to that demonstrated in Fig. 1 for β-cristobalite. Reversible structural changes occur for temperatures sufficiently below T_m, which probably happens up to the temperature with an almost linearly increasing potential energy. It is evident from the 0 and 37 ps insets of Fig. 1 that the tetrahedra of the crystalline structure progressively distort, although bonds are not readily broken until the temperature T_m is reached, which is therefore identified as the melting point. This occurs at $T_\mathrm{m}=8150$ K, but the value depends on the starting configuration, heating rate, and restrictions. In contrast to NpT ensembles NVE simulations show jumps in the pressure when the heating is started and at the beginning of the melting process. Around T_m, the NpT ensembles show a strong volume reduction and an instability of p, followed by relaxation. After amorphization, the sample is heated to 10^4 K to ensure a good atomic mixing. A snapshot of the melt shortly before the amorphous structure is frozen is given by the 217 ps inset. The intersection of the slopes of the upper and lower cooling curves at $T_g=2900$ K represents the glass transition point T_g. There the molecular motions of the material slow down considerably. Melting point T_m and glass transition temperature T_g in Fig. 1, as shown by the intersecting lines or that of the slope, respectively, have much higher values than those obtained experimentally. This discrepancy is thought to be due to differences in the heating rates of simulated and actual glasses and to the fact that the crystalline starting model does not have comparable defects to initiate the melting process. Therefore and for the sake of comparability of all results, in the following the temperatures are scaled with the fictive glass transition temperature T_g of the corresponding simulation, i.e., $T_g=2900$ K in model N3P2 (cf. Table I).

In addition to the model N3P2 described above, β-cristobalite and β-tridymite were heated to T_m at 2×10^{14} K/s and quenched at different rates. Some of the results are summarized in Table I. The T_g values, short-range

TABLE I. Characterization of some typical a-silica models (potential parametrization: N#P1,[a] N#P2[b]) obtained by applying different cooling rates and pressures during MD annealing: Resulting glass transition temperature T_g and density ρ, relative rate Q_n of Si with n oxygen bridges, rates O_1 and O_3 of one- and three-fold bonded oxygens, and relative number of three-fold rings.

Model	Cooling rate (K/s) Pressure (GPa)	T_g (K) ρ (g cm^{-3})	Q_3	Q_4	Q_5	O_1 O_3	Three-fold rings
N5P1	2×10^{15}	3400	0.028	0.954	0.018	0.014	0.189
	5	2.76				0.023	
N6P1	2×10^{14}	3860	0.014	0.977	0.009	0.005	0.106
	5	2.75				0.007	
N8P1	8×10^{12}	3440	0.0	0.982	0.018	0.0	0.111
	5	2.75				0.009	
NlowP1	1×10^{13}	4100	0.008	0.985	0.008	0.004	0.098
	1	2.08				0.008	
N1P2	2×10^{15}	3210	0.0	0.958	0.042	0.0	0.167
	5	2.83				0.021	
N3P2	2×10^{13}	2900	0.005	0.981	0.014	0.002	0.069
	5	2.88				0.009	
N9P2	8×10^{14}	3310	0.014	0.963	0.023	0.007	0.227
	5	2.85				0.019	

[a]See Ref. 8.
[b]See Ref. 25.

order, number and type of defects, angle and ring distributions are influenced by the BMH parameters chosen[24] as well as by the annealing temperature and rate. To understand the effect of different potentials, two sets of a-SiO_2 models were created (see Refs. 8 and 25) and denoted by N#P1 and N#P2, respectively. Samples N#P2 tend to have more defects, lower T_gs and T_ms, and higher densities than N#P1 samples: Our simulations yield good average values of the glass temperature and density, viz. $T_g=3100\pm200$K and $\rho=2.88$ g cm^{-3} for the samples N#P2, $T_g=3600\pm200$ K and $\rho=2.77$ g cm^{-3} for models N#P1, and $T_g=4100\pm200$ K, $\rho=2.08$ g cm^{-3} for the lower-pressure simulations (see, e.g., NlowP1). However, the cooling rates influence these values, and faster cooling rates tend to cause a larger number of smaller rings and more defects than slower rates. Furthermore, the cooling rate and the pressure applied influence the number of coordination defects.[26] Broken bonds especially change the ring structure and the connection of the Si via the O bridges. One broken bond may result in the reduction of the number of O bridges from 4 to 3, in the perfect structure and at the defect site. Such silicon atoms are known as Q_3 species (generally, Q_n if n other Si are bonded via O bridges). Therefore, Q_n with $n\neq4$ and the reduction of the number of Q_4 species are characteristics of regions with defects (as of the surface, too, see Sec. III B). Similar explanations hold for the oxygen bonding states, denoted by O1 and O3 in Table I, as well as for the ring arrangement, described by the relative number of the silicon atoms in the threefold rings. These rings consist of exactly three linked –Si–O– groups in the bulk. In the simulated examples of Table I model N1P2 solely showed two-fold rings (0.9%). Figure 2 demonstrates the effect of melting on the internal ring structure. For the sake of evidence the rings are analyzed here for a selected layer of the model about 0.6 nm in thickness. It is important later on to determine analogously in layer structures the local variation of the rings, the Q species, and thus the defects as a function of the depth below the surface. Note the projection of the six-fold rings in the crystalline material [Figs. 2(a) and 2(b)] and the corresponding distortions in silica [Figs. 2(c) and 2(d)]. The data in Table I reflect the increase of bonding defects with the cooling rate relative to pressure and potential parameters. Figure 2(e) demonstrates this more explicitly for the Q_4 species as a function of the cooling rate. The number of Q_4 is roughly proportional to the negative logarithm of the cooling rate.

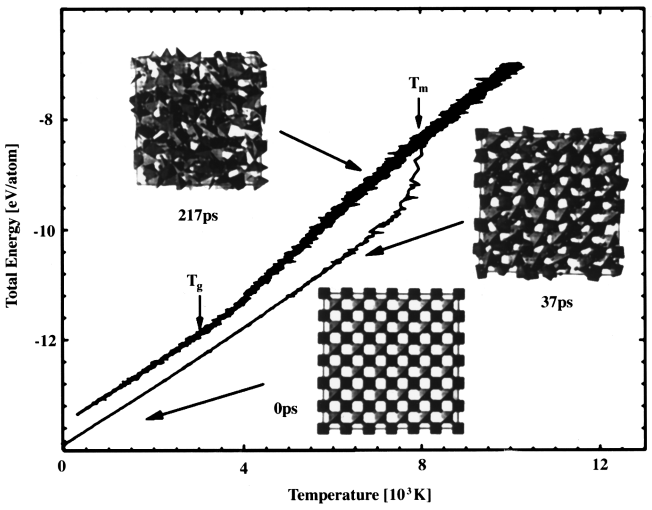

FIG. 1. MD glass generation by annealing: total potential energy per atom of the simulated system as a function of the temperature. Insets: structural models of the crystal at low temperature (0 ps), slightly below melting (T_m, 37 ps), and of the melt (217 ps) near the glass transition T_g.

Bond angle and bond length distributions of both groups were generally the same if values of the whole bulk models were examined. Differences occurred at surfaces and in defect regions. Figure 3 shows the bond angle angular distribu-

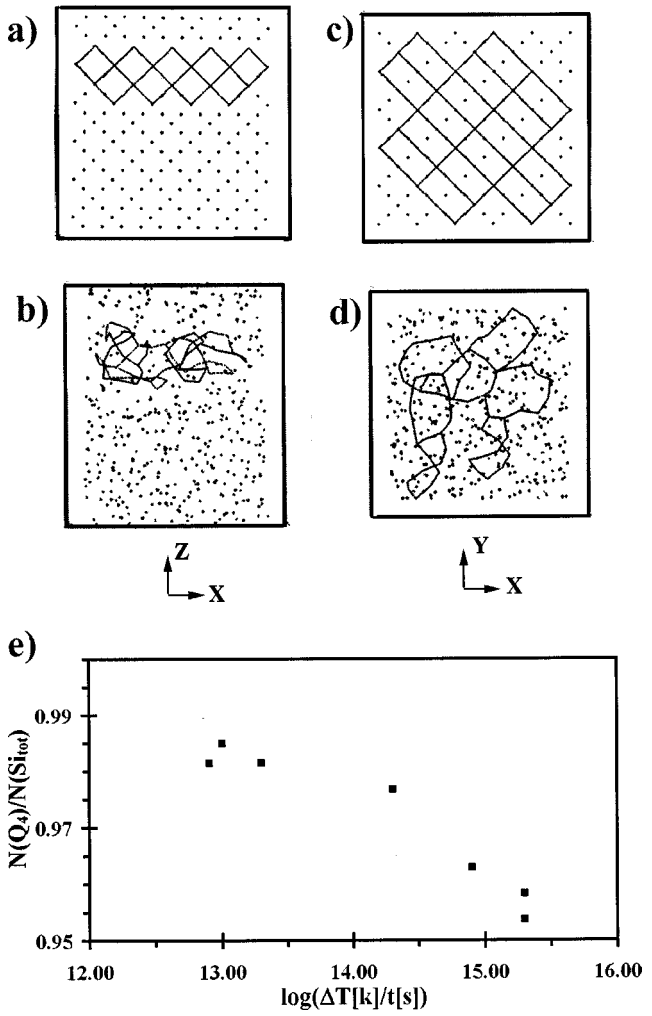

FIG. 2. Determination of the six-fold ring structure [(a),(b) cross sections; (c),(d) plain views] in one selected layer of *c*-silica (a),(c) and *a*-silica (b),(d), and corresponding number of Q_4 species as a function of the cooling rate (e).

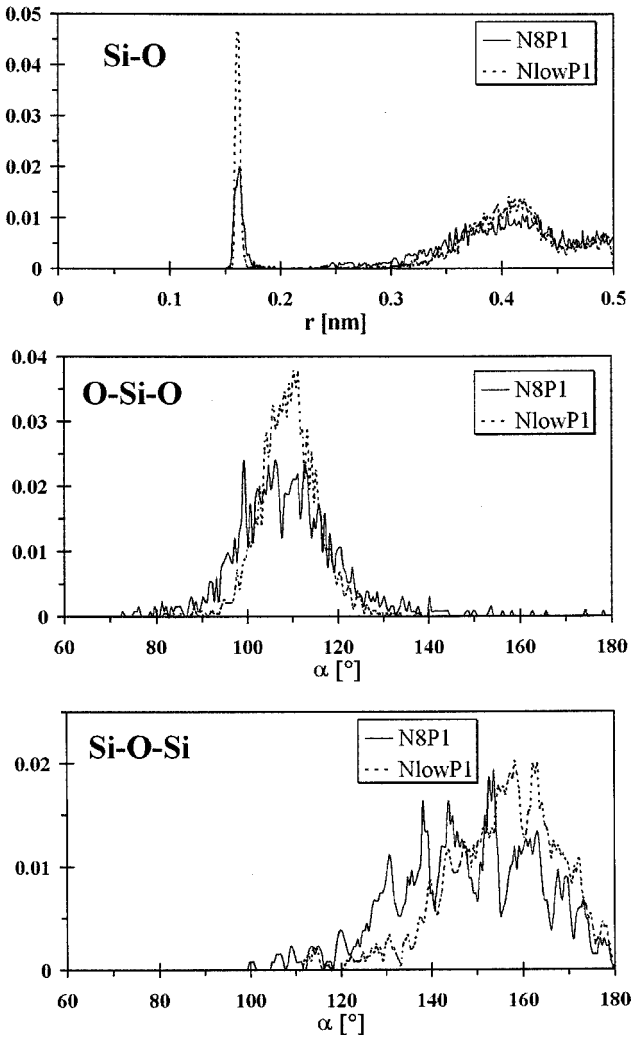

FIG. 3. Influence of the annealing regime on the resulting glass structure: Si–O PDF, O–Si–O ADF and Si–O–Si ADF of glass models N8P1 and NlowP1 (see Table I).

tion function (ADF) and length distributions pair distribution function (PDF) of two structures under different annealing regimes. Before annealing, the distances and the angular distribution are sharp as characterized above for β-cristobalite. For temperatures below T_m (regime of reversibility) the same data describe the average values of bonds and angular distributions, however, at increasing variance (see β-tridymite data). Typical silica glass structures, however, may be characterized as follows: Si–Si=0.315±0.013 nm, Si–O=0.161 ±0.002 nm, O–Si–O=108.8±4.8°, Si–O–Si=157.2 ±17.4°, where T_m is in the range of $1.5T_g$–$2.5T_g$. The most important differences occur for the Si–O distances, shifted approximately 10% to higher values, and the lowered Si–O–Si angular peak reduced by about 30% with respect to the crystalline structure. The distributions are not symmetric with respect to the mean values, and a lower pressure or a higher cooling rate seems to increase the peak shift and to broaden the distributions. The structures generated at higher pressures are preferred in the following because they better reveal the experimental density. This is important solely for the diffusion processes and results from a sufficiently fast equilibration similar to the problem of high melting and glass transition temperatures discussed above. A comparison with low-pressure annealing (as for NlowP1 of Table I) showed that there is no remarkable influence on the simulation of the bonding process itself as will be discussed in Sec. III B.

B. Free silica surface

Free surfaces were generated from annealed glass models using further relaxation at a constant volume by extending the simulation box in the *z* direction, with reflecting walls at the top and bottom of the cell, and applying periodic boundary conditions in the *x* and *y* directions. Hereby, the bottom third of atoms in the *z* direction was frozen to room temperature by rescaling the particle velocities according to the temperature differences. This resulted in a lower heat flux from the surface into the bulk and enabled structural relaxations because of the surface or reaction energies gained.

Most of the dangling bonds at both *z*-directed surfaces, generated by switching off the periodic boundary conditions, recombine in a very short period. In this way, a mainly oxygen-terminated surface had formed, with some of the silicon atoms connected to only three other silicons via bridging

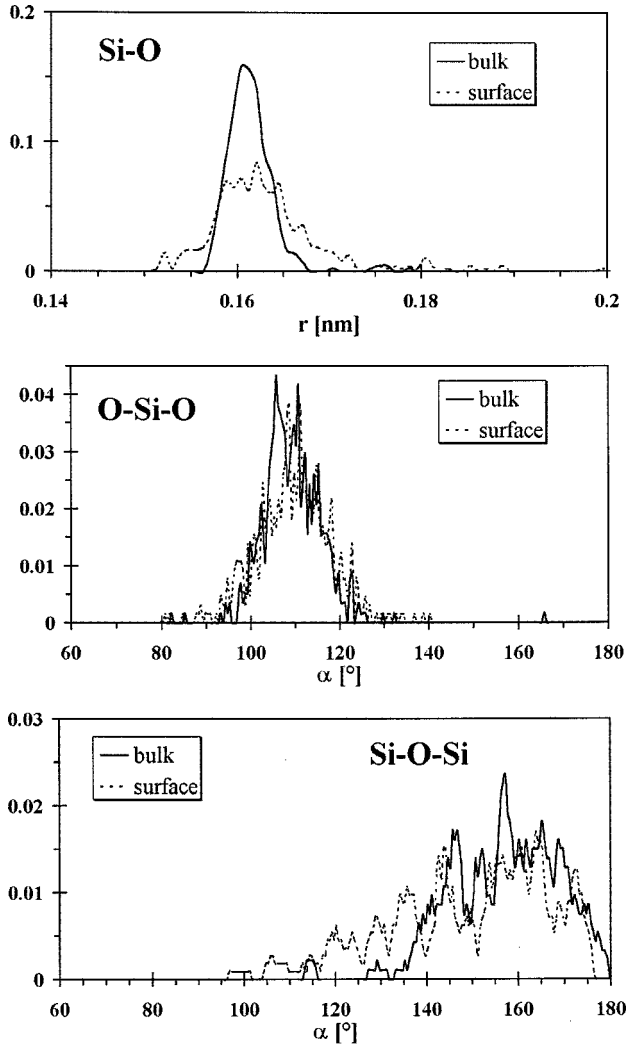

FIG. 4. Structural changes of the *a*-silica from the bulk to the surface layer comparing the Si–O PDF, O–Si–O ADF and Si–O–Si ADF distributions.

oxygens. Thus the number of Q_3 species at the surfaces is higher than in the bulk. Because of the dangling oxygen atoms or the free silicon valences, which are related to these Q_3 species, these sites are expected to have a higher surface reactivity. Besides, the reconstruction also leads to a high density of three-fold rings near the surface. Such rings are hardly ever found within the bulk structure (see Table I). Since the number of three-fold membered rings is larger at the surface than in the bulk, the average angle and length distributions of the surface layer versus the bulk will be different. These differences are related to higher bond energies and could therefore be a reason for increased surface reactivity too. In contrast to other simulations[6,24] no remarkable amounts of two-fold rings were obtained here for low density structures (NlowP1, $<2\%$ two-fold rings). However, surfaces of high-density structures show two-fold rings up to 40%. Instead of the ring behavior, Fig. 4 shows the changes of the PDF and the ADF's for the bulk and the surface layer of the model. The distribution functions can be directly compared with Fig. 3. Near the surface the distributions are broadened and the angular peaks are shifted toward lower values (see also Refs. 6, 24 and 27 and references therein).

After relaxation, the reconstructed surfaces were bombarded with H_2O groups. Some relevant simulations are summarized in Table II: 20–80 water molecules with an energy of 0.5–5 eV and a rate of 0.5 molecules/ps were randomly deposited on the surface by allowing them to settle and react with it. H_2O groups with energies of up to 1 eV became attached to the surface mostly by hydrogen bonding (see Table II, models I and II). There they formed clusters or chains. At higher energies, some H_2O molecules reacted with the silicate surface to create silanol SiOH- and free H or OH groups, which are connected to the surface or other H_2O molecules via H bonds. At 3 eV, the maximum number of SiOH groups form (IV). Higher impact energies result in a stronger dissociation of water, implying however, a smaller amount of silanols (V) forming. In order to simulate a uniform hydrogen-bonded water layer at the surface, the 3 eV impact energy model is subsequently bombarded with 60 1 eV H_2O molecules (VI, VII). The deposition behavior and the resulting silanol/water layers are also influenced by free oxygen radicals created by fragmentation or additional deposition. This, however, will be discussed in a forthcoming paper.

The snapshots of Fig. 5 characterize the reaction of water with the silica surface. First, water clusters form. The overlap of the clusters, however, results in a homogeneous water layer [Fig. 5(a)] with a silanol density comparable to the experimental ones. The simulation time applied is too short for the recombination of the reaction products of the silanol formation, i.e., some of the H and OH remain free. The water bombardment of the surface initiates only small changes in the silica structure. In Fig. 5(b), the upper surface

TABLE II. Adsorbates on silica surfaces after water deposition (starting from NlowP1): Distribution of molecule fragments [Si(OH), $Si(OH)_2$, H_2O, OH, H] as a function of the deposition energy and rate (energy and number of H_2O deposited).

Model	Starting structure	Energy (eV)	H_2O deposited	Si(OH)	$Si(OH)_2$	H_2O	OH	H
I	free surfaces	0.5	20	2	1	14	4	4
II	free surfaces	1	20	5	1	11	5	6
III	free surfaces	2	20	6	0	8	8	10
IV	free surfaces	3	20	12	2	5	7	7
V	free surfaces	5	20	8	0	3	12	14
VI	model IV	1	50	12	4	30	11	9
VII	model V	1	80	14	4	59	12	8

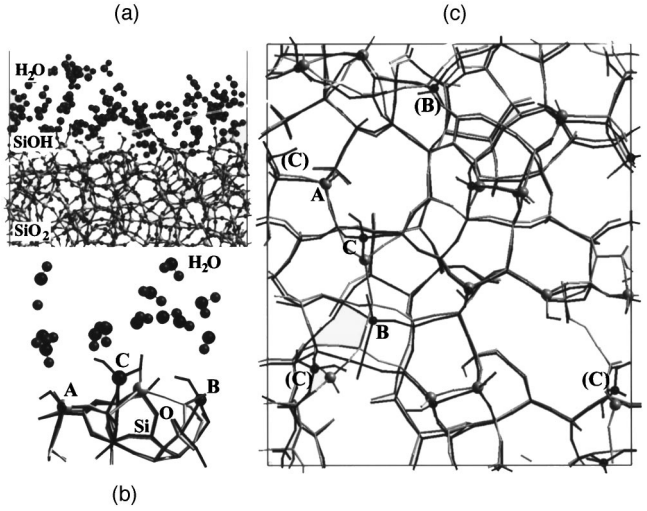

FIG. 5. Silica surface after H_2O bombardment (model VII): (a) side view (silica: ball and stick model; water: larger balls), (b) matched top view of a silica surface layer before (grey) and after water treatment (black): Solely Q_3 sites and Si of silanols are displayed as balls at the pure and the hydroxylated silica surface, respectively (free hydrogen and water molecules are omitted in the stick model; the different reactions at A, B, C are bond saturation, siloxane breaking and geminal group generation, respectively), (c) side view of the matched surface structures of (b) cut along A, C, B.

layer of the free relaxed silicate glass (light grey) and the corresponding hydroxylated structure (model VII; black) are matched and viewed in normal projection to the interface. Figure 5(c) shows a magnified part of the area marked by A, C and B. Again, both models are projected into the same plot, but now as a cross section of the interface. In these stick models only the Q_3 species and those silicon atoms with bonded OH groups are represented by small balls for the pure surface and the hydroxylated one, respectively. All the other Si atoms can be revealed solely by the crossing bonds via oxygen. Obviously, the silica network has changed only slightly. Two main processes are distinguishable: First, after dissociation, most of the water reacting with the surface is bonded to the Q_3 groups. Thus dangling bonds are saturated without breaking any Si–O bond [Figs. 5(b) and 5(c) site A and all nonmarked sites with black balls are of this type). Second, only a small number of H_2O groups is able to cleave the strong Si–O–Si bridges, i.e., to break the siloxane bonds. This preferably happens to Si–O–Si groups, which are part of three- or four-fold rings (sites B). The destruction of the Si–O–Si bridge (siloxanes) results not only in the formation of two silanol groups but also in a relaxation of the adjacent network. Furthermore, both the Q_3 saturation and the breakage of siloxane results in multiple silanols (see sites C, called geminal groups in Ref. 28). The particular reactions and especially the arrangement of the twofold silanols at site C are directly shown in the magnified detail of Fig. 5(c).

C. Silica bonding behavior

Two adjoining hydroxylated surfaces, each covered with 1–2 monolayers of water (e.g. surface model VII) are brought into contact to simulate the wafer bonding between silica and/or hydrophilic Si. Figure 6 shows snapshots of the interface at different temperatures and simulation times similar to those in Ref. 6: (a) initial configuration, $0.125T_g$, 30 ps, (b) $0.7T_g$, 110 ps, (c) $1.6T_g$, 40 ps, (d) $0.8T_g$, 250 ps. Note the breakup of the surface, particularly at $1.6T_g$. Longer and shorter silica strands loosen from the surface and migrate into the gap. This bridging effect occurred not only at temperatures higher than T_g but also during long time simulations at $0.8T_g$, [Fig. 6(d)]. The many open spaces indicate that smaller portions of the surface have broken from this layer and most probably migrated into the gap. Pits formed in one area of the surface through the action of temperature and pressure help form bridging covalent bonds in other sections of the wafer.

The processes and the resulting surface roughening can be studied in detail using the calculated density plots across

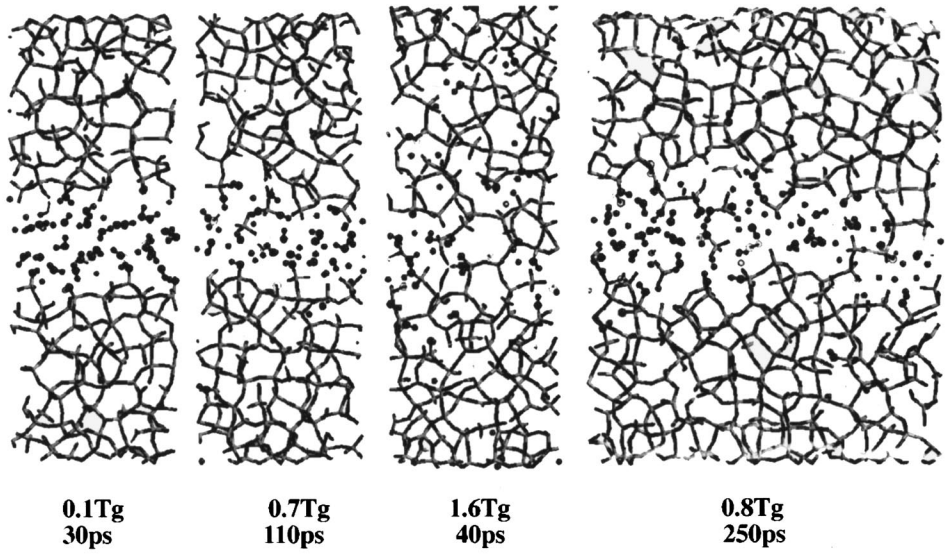

FIG. 6. Snapshots of MD simulations of hydrophilic wafer bonding at different tempering temperatures and simulation times: $T=0.1T_g$, $t=0$ ps; $T=0.7T_g$, $t=110$ ps; $T=1.6T_g$, $t=40$ ps; and $T=0.8T_g$, $t=250$ ps.

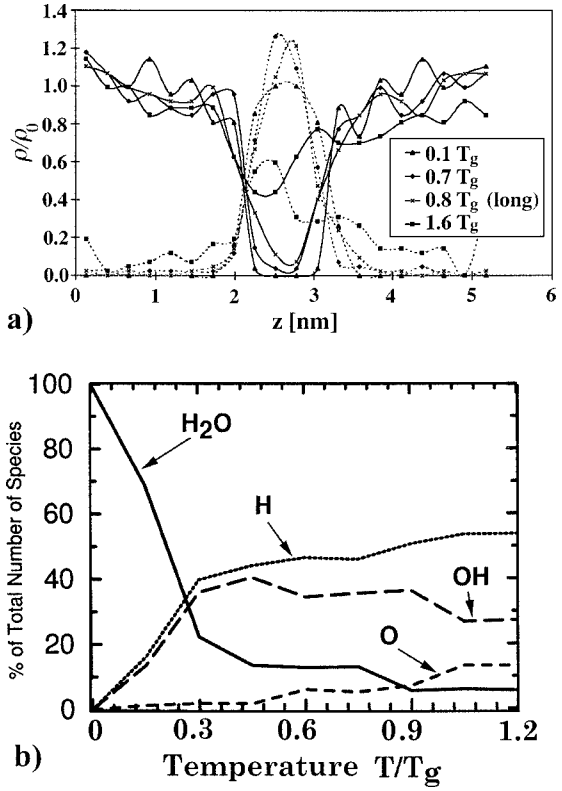

FIG. 7. Structural changes at the bonded interface: (a) normalized averaged density ρ/ρ_0 ($\rho_{0,\mathrm{Si}}$: Si bulk density; $\rho_{0,\mathrm{H}}$: initial H density in the gap) of the atomic species (Si: full line, H: dotted line) perpendicular to the interface for the differently tempered models of Fig. 6, (b) dissociation of the water within the interface gap as a function of the temperature.

the interface, and monitoring the H_2O dissociation (see Fig. 7). Figure 7(a) shows the variation of the Si and the H density through the interface in the *z* direction for different temperatures corresponding to Fig. 6. The stepwise transition of the density for lower temperatures is broadened at higher ones and corresponds to the hydrogen diffusion zone. In addition, the dissociation of the water groups within the gap is plotted as a function of the temperature [Fig. 7(b)]. In general, at temperatures below approximately $0.3T_g$, the rapid breakage of H_2O groups with the formation of H and OH is obvious. However, the mobility of these connected and free H ions is restricted to the *x* and *y* directions, i.e., along the

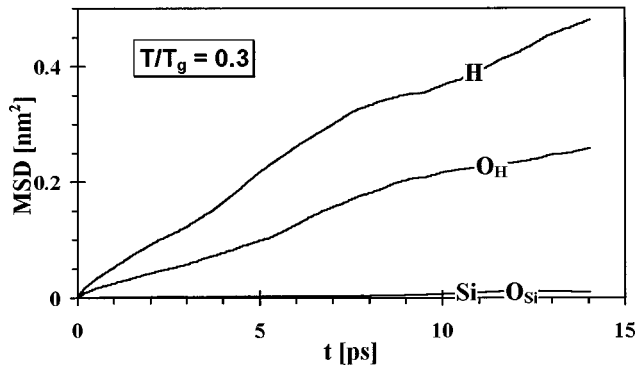

FIG. 8. MSD functions of the bonded silica interface structures for different atomic species (oxygens in H_2O and SiO_2 distinguished).

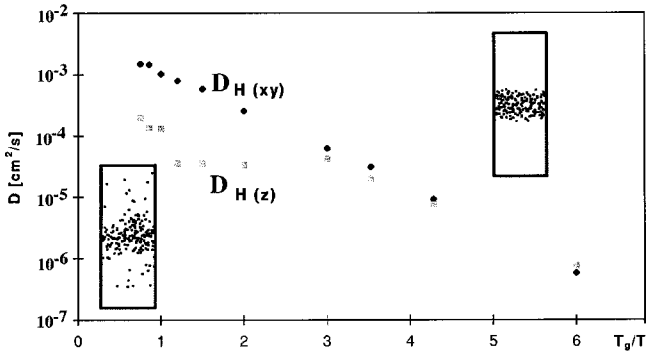

FIG. 9. Arrhenius plot of the hydrogen diffusion coefficients D_{H} in a bonded silica interface structure perpendicular (*z* direction) and parallel (*xy* direction) to the interface. Insets: x projection of the H atoms at $0.3T_g$ and $1.1\ T_g$.

wafer surface they cannot enter the bulk. Near T_g the OH groups begin to break, too. The smaller H and O groups can diffuse into the bulk more easily. Coupled with the fragmentation and opening of the surface, an increase of the diffusion constant of hydrogen for the *z* direction is obtained. As will be shown below (see Figs. 9 and 10) this diffusion process influences the wafer bonding behavior.

D. Bond breaking and diffusivity of adsorbates

Figure 8 shows the MSD function of all atomic species in the gap at about $0.3T_g$ for a typical MD bonding situation. In order to emphasize the movement of the H_2O molecules, oxygen (O_{Si}) bonded to silicon in the bulk structure, and oxygen (O_{H}) bonded to hydrogen in the gap, will be considered separately. After a very short parabolic section (0.1 ps) the functions reveal a rough linearity. While hydrogen and oxygen within the gap are quite mobile and indicate a translational movement, the small MSD values ($>(0.1\ \mathrm{nm})^2$, but smaller than the square of the Si–O distance) of silicon and oxygen within the bulk result from a purely vibrational movement. The slope of the MSD functions enables the evaluation of the diffusion constant *D*, using the Einstein relation:

$$D = d/dt\ [\langle (r - r_0)^2 \rangle / 2N],$$

where $N=1$ for the diffusion in one direction, $N=2$ for the diffusion in a plane, and $N=3$ for a three-dimensional diffusion. This calculation, however, only makes sense for the hydrogen and the oxygen diffusion with the assumed strong translational movement.

Figure 9 shows the diffusion of the hydrogen atoms in the *z* direction, i.e., perpendicular to the gap, as well as in the *xy* plane, i.e., parallel to the gap, for temperatures between $0.17T_g$ and $1.4T_g$. In the *xy* direction, the hydrogen movement results in a nearly linear temperature dependence within the Arrhenius plot. This reflects an ideal diffusion behavior along the gap with probably no significant disturbances at any temperature. For the diffusion perpendicular to the gap, three different regions can be identified. For lower temperatures up to $0.3T_g$, the diffusion values as well as the linearity of the plot are comparable with the *xy* diffusion. Here, because of the relatively short MSD times, mainly the

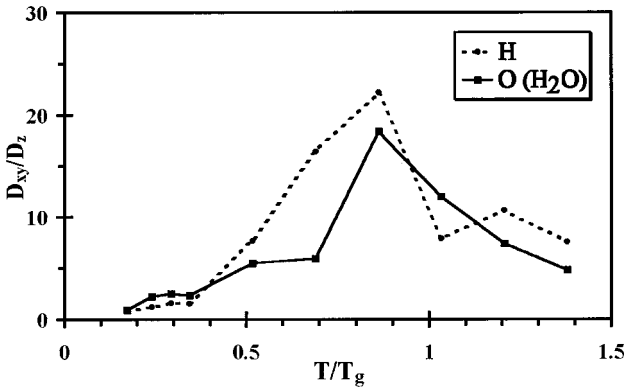

FIG. 10. Ratio of the diffusion coefficients of H and O within water and its dissociation fragments calculated for the bonded silica surface as a function of the temperature.

movement within the gap is measured. At temperatures between 0.3 and $0.9T_g$ the diffusion is approximately constant. This means that the water–silica interface seems to be a strong barrier to the hydrogen diffusion, which can be overcome only at temperatures above T_g. Between T_g and $1.4T_g$ the diffusion constant increases rapidly, revealing a different diffusion mechanism. The inserts of Fig. 9 show typical snapshots of the diffusion of H into the silica materials at the temperatures of 0.3 and $1.4T_g$. Note that here hydrogen is not distinguished to belonging either to the H, the OH or the H_2O group. The diffusion into the bulk is remarkable solely above $0.9T_g$.

The diffusion of water molecules, oxygen ions, and OH groups is measured by the movement of oxygen within the gap. It results in a diffusion similar to that of hydrogen, however, with at least one order of magnitude lower diffusion constants. Only at temperatures near or above T_g do the diffusion values deviate from a linear Arrhenius behavior. This indicates the start of the bonding process, which also inhibits the oxygen diffusion in the *xy* direction. In the *z* direction again three sections within the diffusion curve can be recognized enabling a similar interpretation for hydrogen. It also must be emphasized that at elevated temperatures the diffusion constant in the *z* direction for hydrogen is about eight times higher than that of oxygen.

To sum up the diffusion behavior in Fig. 10, the ratio D_{xy}/D_z of the *xy* and *z* directed diffusion is shown for both the H and O species. Below approximately $0.3T_g$ the movement of H and H_2O within the gap is nearly isotropic, i.e., the diffusion constants are independent of the direction. The mean free path reaches the order of the gap width at about $0.6T_g$, resulting in a strong increase in the ratio D_{xy}/D_z. Suitable MD measurements (half width of the gap density Fig. 7, and maximum change of the MSD slope in Fig. 8) yield average diffusion lengths of 0.28 nm for H_2O and 0.35 nm for H. The corresponding mean free path of 0.027 and 0.12 nm, respectively, given by the theory of an ideal gas at a temperature of $0.6T_g$, are much smaller, and indicate that the simulated diffusion lengths reflect the gap width.

At the strong maximum around $0.9T_g$, the diffusion in the *xy* direction is more than 20 times higher than in the *z* direction. For higher ($>1.2T_g$) temperatures the diffusion into the bulk is nearly of the same order of magnitude as the diffusion along the interface. In this temperature range the bulk diffusion should be the most essential process, especially because of the very long diffusion paths to the wafer edges. A rough estimation of the experimental diffusion paths into the wafer (on the order of 10 nm) and out of the edges of a wafer (on the order of 1 cm) shows that the ratio D_{xy}/D_z has to be at least on the order of 10^{13}–10^{14} for a preferred water removal out of the water edges. Extrapolating the MD calculated ratios for $T \geqslant 0.9T_g$ to lower temperatures this can only be reached for temperatures lower than $T \approx 400$ K.

By analyzing the vibrational spectrum (which will be done in detail in a forthcoming paper) these results may be confirmed and directly related to experimental infrared (IR) and Raman spectra.

IV. DISCUSSION

Although only one silica polymorph is stable in classical MD using the BMH potential, sufficiently good silica glasses can be created. Future work will consider other potentials and especially modified embedded atomic approximations to enhance the structure generation and to enable the Si/SiO_2 interactions. These relaxed silica glasses have a highly reactive surface. Water molecules settling on the surface have at least three different kinds of bonding sites. They correlate to sites attached to Q_3, or where silanols are created by cracking Si–O bonds in the surface. Further water molecules are bonded via hydrogen bonds. A deposition energy of approximately 3 eV yields a good hydroxylation of the surface. Subsequent bombardment with oxygen leads to the dissolution of water and the separation of hydrogen. The reactivity is a function of the Q_3 density and of the number of three-fold rings, which both describe the defect structure of the surface.

The activated and relaxed surfaces covered with silanol and water form the basis for the simulation of silica wafer bonding, which can be used as a model of the hydrophilic Si wafer bonding. There are three different regimes, which can be related to experimental observations.[29] The short-time behavior at low temperatures and pressures leads to hydrogen-bonded surfaces with a low bonding energy. The bonding energy can be increased either by increasing the temperature and/or the pressure, or by tempering at lower temperatures for sufficiently long times. Increasing the temperature and/or pressure enables us to dissolve the silanol and water groups and to lower the diffusion barriers. Thus the interface gap can be closed by forming direct silica–silica bonds. The long time behavior shows a reactive rearrangement of the surface, which locally leads to strong silica bonds even at low temperatures (e.g., at $0.6T_g$ within some ps). However, the relation between these different bond regimes and the experimentally observed bond energy plateaus is incomplete, as in our present model the water, OH and oxygen diffusion is described without the oxidation of the bulk Si. Nevertheless, the oxidation as well as the movement of the oxidation reaction front may influence the diffusion. It has to be the most important process because the oxide is much thinner than a possible diffusion length along the bonded interface.

V. CONCLUSIONS AND SUMMARY

Molecular dynamics simulations based on empirical potentials are used to investigate the elementary steps of bonding two silica surfaces. MD simulations show that the most crucial problem consists in finding complex atomic potentials covering bulk and surface structures as well as the interaction with adsorbates. The resulting bond energy depends on the assumptions of the molecular dynamics modeling as, e.g., heat transfer, annealing temperature, and surface treatment. Water molecules are reacting with the siloxane bonds thus forming silanol layers. The structure of further water layers is determined by external forces and the kinetic energy of H_2O as well as by all the various fragments having formed during the reaction. The critical energy barrier to transform hydrogen bonds to covalent Si bridges is related to the surface roughness and the diffusivity of the adsorbates, and is thus mostly controlled by the annealing temperature.

[1] K. Scheerschmidt, D. Conrad, A. Belov, and U. Goesele, Comput. Mater. Sci. **9**, 108 (1997).
[2] K. Scheerschmidt, D. Conrad, A.Belov, and H. Stenzel, Proceedings of the 4th International Symposium on Semiconductor Wafer Bonding: Science, Technology, and Applications, edited by U. Gösele *et al.*, 1998, Pennington, Electrochemical Society Proceedings, Vol. 97–36, pp. 381–392.
[3] D. Conrad, K. Scheerschmidt, and U. Gösele, Appl. Phys. A: Mater. Sci. Process. **62**, 7 (1996).
[4] D. Conrad, K. Scheerschmidt, and U. Gösele, Appl. Phys. Lett. **71**, 2307 (1997).
[5] A. Y. Belov, D. Conrad, K. Scheerschmidt, and U. Gösele, Philos. Mag. A **77**, 55 (1998).
[6] S. H. Garofalini, Proceedings of the of 2nd International Symposium on Semiconductor Wafer Bonding: Science, Technology, and Applications, edited by M. Schmidt *et al.* 1994, Pennington, Electrochemical Society Proceedings, Vol. 93–29, pp. 57–70.
[7] E. Webb and S. H. Garofalini, J. Non-Cryst. Solids **226**, 47 (1998).
[8] B. P. Feuston and S. H. Garofalini, J. Appl. Phys. **68**, 4830 (1990).
[9] D. Timpel, K. Scheerschmidt, and S. Garofalini, J. Non-Cryst. Solids **221**, 187 (1997).
[10] H. Kageshima and K. Shiraishi, Surf. Sci. **380**, 61 (1997).
[11] J. R. Chelikowsky, N. Troullier, J. L. Martins, and H. E. King, Phys. Rev. B **44**, 489 (1991).
[12] B. Silvi, M. Allavena, Y. Hannachi, and P. D'Arco, J. Am. Ceram. Soc. **75**, 1239 (1992).
[13] C. R. A. Catlow and A. N. Cormack, Int. Revs. Phys. Chem. **6**, 227 (1987).
[14] F. H. Stillinger and T. A. Weber, Phys. Rev. B **31**, 5262 (1985).
[15] A. Rahman, F. H. Stillinger, and H. Lemberg, J. Chem. Phys. **63**, 5223 (1975).
[16] S. H. Garofalini, J. Non-Cryst. Solids **120**, 1 (1990).
[17] S. Tsuneyuki and Y. Matsui, Phys. Rev. Lett. **74**, 3197 (1995).
[18] P. Vashishta, R. K. Kalia, A. Nakano, and W. Jin, Int. J. Thermophys. **17**, 169 (1996).
[19] M. I. Trioni, A. Bongiorno, and L. Colombo, J. Non-Cryst. Solids **220**, 164 (1997).
[20] S. Carniato, G. Boureau, and J. Harding, Radiat. Eff. Defects Solids **134**, 179 (1995).
[21] N. R. Keskar and J. R. Chelikowsky, Phys. Rev. B **46**, 1 (1992).
[22] T. P. Swiler, J. M. Simmons, and A. C. Wright, J. Non-Cryst. Solids **182**, 68 (1995).
[23] I. P. Swainson and M. T. Dove, J. Phys.: Condens. Matter **7**, 1771 (1995).
[24] B. P. Feuston and S. H. Garofalini, J. Phys. Chem. **94**, 5351 (1990).
[25] D. C. Athanasopoulos and S. H. Garofalini, J. Chem. Phys. **97**, 3775 (1992).
[26] R. Car and M. Parrinello, Phys. Rev. Lett. **60**, 204 (1988).
[27] M. Rovere, M. A. Ricci, D. Vellati, and F. Bruni, J. Chem. Phys. **108**, 9859 (1998).
[28] A. M. Ferrari, P. Ugliengo, and E. Garrone, J. Phys. Chem. **97**, 2671 (1993).
[29] U. Gösele and Q.Y. Tong, Ann. Rev. Mater. Sci. **28**, 215 (1998).